Self-Turning Process and Aerodynamic Characteristics of Slender Bodies with Different Center-of-Gravity Positions

X. Gu[1], C. Liu[1†], Y. Zhang[2] and H. Jiang[1]

[1] *School of Mechanical and Automotive Engineering, Shanghai University of Engineering Science, China*
[2] *Shanghai Academy of Spaceflight Technology, China*

†*Corresponding Author Email: liucf@fudan.edu.cn*

ABSTRACT

To achieve an automatic technology for over-the-shoulder (OTS) launching of air-to-air missiles, this study numerically simulated the overturning process of a slender body by using the dynamic mesh method in the ANSYS Fluent 2021 software. Motion trends and force conditions during the self-turning process were obtained for different center of gravity positions. This investigation showed that a proper center of gravity position was essential for achieving the self-turning of a slender body at high and extra-wide angles of attack. The pressure center of the slender body jumped (discontinuously changed) during the overturning process. The change in the relative position between the pressure center and the center of gravity caused the angular velocity of the slender body to first increase, then decrease and gradually stabilize. These results can be used as a reference for designing the structures of self-turning slender bodies and to realize a new technology for the OTS launching of air-to-air missiles.

Keywords: Self-turning; Dynamic mesh; Pressure center; Missile; Center of gravity.

1. INTRODUCTION

With upgrades in air combat scenarios, capable over-the-shoulder (OTS) launching has become an essential operational performance for modern air-to-air missiles. An OTS launch can effectively improve a fighter's ability to attack a rear-hemisphere target and can significantly influence the survivability of the fighter on the battlefield (Ma and Li 2020). Importantly, there are two OTS launching methods (forward and backward) for air-to-air missiles mounted on fighters. A forward launch is a normal missile launch, after which the missile turns in the air to attack a rear target. The existing forward launching methods primarily use pure aerodynamic turning or direct force-controlled turning, and their launch times are approximately 8 and 3 seconds, respectively (Thukral and Innocenti 1998). A backward launch changes the missile direction by rotating the launch mount before launching the missile. These turning methods are problematic because of their long combat response times. To shorten the combat response time when launching an air-to-air missile (to only one second), this paper proposes a method that uses a self-turning technology for a slender body to achieve OTS launching. This new launching technology is expected to improve the agility of air-to-air missiles and the survivability of fighters.

In general, this new self-turning technology uses the effect of the aerodynamic force on a statically unstable missile with an extra-wide attack angle to achieve overturning and reorientation of the missile when it is separated from the fighter. The unstable state is predetermined and controllable and can quicken the missile turning attack without sacrificing stroke durability.

During a self-turning OTS launch, with a gradually increasing attack angle, the missile experiences wide and extra-wide attack angles, and the aerodynamic characteristics of its external flow field become a complex unsteady problem (Li *et al.* 2017). Teng (2018), Hechmi and Taieb (2012), Barnette *et al.* (2012), Liu (2018), and Howison and Ekici (2013) explored this problem using wind tunnel tests and numerical simulations. Their results show the eddy current and hysteresis effects in the flow fields of axisymmetric slender bodies at subsonic and transonic high angles of attack. These effects produce complex wave and vortex system structures. Additionally, the complex flow field caused by vortex shedding affects the aerodynamic characteristics and loads of slender bodies. Le Clainche (2016) studied the formation mechanism of the flow field around the leeward side of a cylinder for different Reynolds numbers and attack angles. After increasing the attack angle, the leeward side turbulence gradually developed into an asymmetric structure and produced a continuously changing side

force on the slender body (Champigny 1986). Zhu *et al.* (2015) and Qi *et al.* (2018) tested and simulated slender bodies with different heads and determined the influence of head protrusion on the side force. Wang (2021) used an asymmetric-tail slender body to calculate the side force in the 0°–90° attack angle range and found that the magnitude and direction of the side force changed periodically during the actual flight process. Deng *et al.* (2016) performed numerical simulations of the uncertainty of side aerodynamic forces at a large attack angle by increasing the inflow pulsation, showing that the side forces during actual flight were far less than the static forces and that they could be used to control maneuverability during flight.

The longitudinal aerodynamic characteristics of a slender body with an extra-wide angle of attack are part of the theoretical foundation for self-turning technology (Yang *et al.* 2011 and Cao *et al.* 2020). At present, the aerodynamic characteristics of this type of slender body with the extra-wide angle of attack have primarily been simulated with a fixed angle of attack, and traditional engineering calculations have not been able to obtain accurate results. Few studies have analyzed the dynamic change in the aerodynamic force as the angle of attack increased. Therefore, this study used the dynamic mesh technique to close the roll and yaw channels when simulating the turning process of a simplified slender body model in the pitching plane. It also investigated the aerodynamic characteristics of a slender body at an extra-wide attack angle in the longitudinal plane and further analyzed the influence of the position of the center of gravity on the aerodynamic characteristics. Finally, a new method of agile steering using pure aerodynamic force was considered, supporting the overall design and the flight control design of air-to-air missiles.

2. SLENDER BODY MODEL

When modeling the missile, the axis of the slender body was taken as the independent variable and one millimeter was used as the variable step for solving the Huck-type function. Then the coordinate point cloud obtained was imported into the three-dimensional modeling software CATIA to generate the warhead curve. This established a simplified model for the slender body, which was composed of the Huck warhead curve and the projectile body. The windward diameter of the slender body is represented by D. The length of the warhead is 2.5D and the size of the projectile body is 17.5D. The slender body shape is shown in Fig. 1.
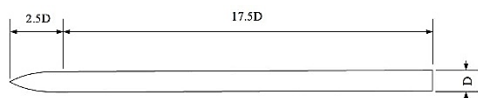

Fig. 1. Slender body model.

Fig. 2 presents a schematic diagram of the slender body flight mechanics model. The angle of attack, *a,* is the angle between the projection of the velocity vector of the center of gravity on the *x*-axis plane of
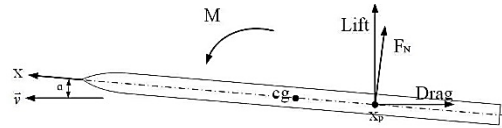

Fig. 2. Schematic diagram of the slender body flight mechanics model.

the projectile and the *x*-axis, M represents the aerodynamic moment, the normal force, F_N, is the normal component of the aerodynamic force, cg represents the position of the center of gravity, and x_p is the pressure center.

The Huck curve function is as follows:

$$r = 150 \times \left[1 - \left(\frac{750 - x}{750} \right)^{2.8} \right] \tag{1}$$

where r is the curve ordinate, x is the abscissa.

3. NUMERICAL SIMULATION METHOD

3.1 Fluid Control Equations

The governing equations are represented by the two-dimensional time-dependent compressible Navier-Stokes equations. The problem discussed in this paper is based on the flow of a single component, and the control equations only include the conservation equations for mass, momentum, and energy. The unified form of the Navier-Stokes equations is shown below.

$$\frac{\partial(\rho\phi)}{\partial t} + \frac{\partial(\rho u\phi)}{\partial x} + \frac{\partial(\rho v\phi)}{\partial y}$$
$$= \frac{\partial}{\partial x}\left(\Gamma \frac{\partial \phi}{\partial x} \right) + \frac{\partial}{\partial y}\left(\Gamma \frac{\partial \phi}{\partial y} \right) + S \tag{2}$$

where ϕ is a general variable that can represent solution variables such as u and v, ρ is the density, u and v are velocity components, μ is the dynamic viscosity, Γ represents the generalized diffusion coefficient, and S is the generalized source term.

The finite volume method with second-order accuracy was selected to discretize the equation in space and time. The nonlinear and unsteady Navier-Stokes equation was then solved. To better simulate transonic shock waves, the advection upstream splitting method (AUSM) was selected to maintain excellent convergence and stability of the dynamic grid calculations, and a composite time integration scheme with second-order accuracy was utilized to obtain an accurate response (Bellakhal *et al.* 2019).

3.2 Turbulent Airflow Model

The Reynolds number is a characteristic parameter of the flow state, and it could be expressed by Eq. (3):

$$\text{Re} = \frac{\rho V D}{\mu} \tag{3}$$

where V is flow velocity and D is the missile diameter.

In the simulations, because the Reynolds number is greater than the critical Reynolds number under

subsonic and supersonic conditions, a turbulence model is introduced to consider the effect of turbulence on the calculated results (Tong *et al.* 2019).

Due to the obvious vortex effect during the overturning process of the slender body, when choosing a turbulence model to simulate the turbulence effect on the flow field, a turbulence model was needed to accurately simulate complex separation phenomena, such as large-scale separation. Therefore, the Reynolds average equation was adopted (Menter 1994). The instantaneous variables in the equation were decomposed into two parts, the average and the pulsation, then a new variable, $-\rho \overline{u_i' u_j'}$, called the Reynolds stress, was introduced. Based on the Boussinesq hypothesis, it was assumed that the Reynolds stress was proportional to the average velocity gradient. Then the eddy viscosity coefficient, μ_t, was obtained by adding parameters such as the turbulent kinetic energy, k, and the dissipation rate, ε Finally, considering the rotation and vortex influences on the turbulent transport and the boundary layer calculations (Kang *et al.* 2020 and Sulaeman *et al.* 2019), the realizable model was selected to complete the solution. This model is presented in Eq. (4):

$$-\rho \overline{u_i' u_j'} = u_t \left(\frac{\partial u_i}{\partial x_j} + \frac{\partial u_j}{\partial u_i}\right) - \frac{2}{3}\left(\rho k + \mu_t \frac{\partial u_i}{\partial x_i}\right)\delta_{ij} \quad (4)$$

where k represents the turbulent kinetic energy and μ_t is the eddy viscosity coefficient. δ_{ij} is a Cornell symbol; when $j = j$, then $\delta_{ij} = 1$, and when $i \neq j$, then $\delta_{ij} = 0$.

$$\mu_t = \rho C \frac{k^2}{\varepsilon} \quad (5)$$

where C is a constant equal to 0.09.

k and ε were calculated using Eqs. (6) and (7), respectively.

k equation.

$$\rho \frac{dk}{dt} = \frac{\partial}{\partial x_i}\left[\left(\mu + \frac{\mu_t}{\sigma_k}\right)\frac{\partial k}{\partial x_i}\right] + G_K - \rho\varepsilon \quad (6)$$

ε equation.

$$\rho \frac{d\varepsilon}{dt} = \frac{\partial}{\partial x_i}\left[\left(\mu + \frac{\mu_t}{\sigma_\varepsilon}\right)\frac{\partial \varepsilon}{\partial x_i}\right] - \rho C_2 \frac{\varepsilon^2}{k + \sqrt{v\varepsilon}} \quad (7)$$

In Eqs. (6) and (7), σ_k and σ_ε are the turbulent Prandtl numbers for the turbulent kinetic energy and its dissipation rate, respectively, and is a constant.

3.3 Flow Field Grid

Simulations were performed on unstructured grids, which were generated using the ICEM CFD meshing tool. The computational mesh is shown in Fig. 3. The larger calculation domain avoided boundary interferences to ensure pressure-far-field boundary conditions. It prevented the slender body from flying out of the calculation domain when turning, which would generate inaccurate results. The movement of the boundary when the slender body overturned caused changes in the mesh. With a substantial reconstruction of the mesh during overturning, the flow field topologies gradually became complicated.
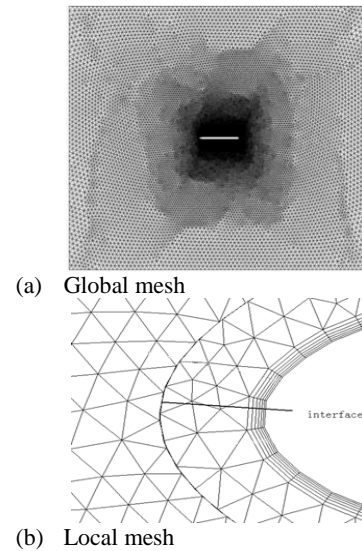

(a) Global mesh

(b) Local mesh
Fig. 3. Mesh Diagram of the simulation.

To avoid calculation failure due to low mesh quality or a negative volume mesh, the mesh around the slender body was encrypted and the number of nodes on the boundary was adjusted to prevent the change rate of the mesh cross-sectional area from being too excessive. The mesh was split into an internal mesh and an external mesh. The internal and external meshes transferred data through their interface to maintain the boundary layer and internal mesh quality while reducing the workload for the boundary layer reconstruction.

3.4 Inflow Condition

Considering the short turning time (within only one second) of the slender body during an OTS launch, the influence of air resistance on the incoming flow conditions of the slender body was ignored in the numerical calculations, and the Mach number during the overturning process was configured as a fixed value. An ideal gas was selected as the fluid domain material, and the pressure-far-field boundary condition was adopted. The inflow conditions are given in Table 1.

Table 1 Flow Conditions of the simulations

Parameter	Height (Km)	Mach number	Atmospheric pressure (Pa)	Temperature (K)	Density (kg/m³)
1	0 (sea level)	0.5	101,325	300	1.1767
2	0 (sea level)	2	101,325	300	1.1767
3	10	0.5	34,146	300	0.3965
4	10	2	34,146	300	0.3965

3.5 Dynamic Mesh Settings

The overturning of a slender body is not a pre-specified motion. By writing a user-defined function, the missile's moments of inertia, mass, and initial angular velocity for a short time were given to the program to simulate the initial flight state after the slender body separated from the fighter. Additionally, the rolling and yaw channels were closed so that the slender body could only move longitudinally. After being given the initial conditions, the slender body moved independently according to the resultant force. The center of gravity coordinates, the angular acceleration, the rotation angle, and other parameters were saved in a specified file. Because of the large displacement of the mesh boundary during the overturning process, it was necessary to combine the elastic smoothing and local mesh reconstruction methods to reconstruct the mesh in the deformation region and ensure that the mesh maintained its high quality.

4. RELIABILITY VERIFICATION OF THE NUMERICAL SIMULATIONS

4.1 Mesh Independence Verification

Mesh independence tests were performed by decreasing and increasing the number of cells by 30%. A medium mesh of near 38,000 cells exhibited good performance. The change in the drag coefficient when the mesh density decreased by 30% was 7.06%. However, when mesh density increased by 30%, the drag coefficient changed by less than 0.17%. This result indicates that refining the mesh did not yield significant changes. Hence, the 38,000-cell mesh was used for further simulations.

4.2 Experimental Comparison

To verify the reliability and accuracy of the numerical method, a test case with a high-Reynolds-number flow past a slender body was evaluated. Adiabatic and no-slip wall boundary conditions were applied to the surface of the slender body, and pressure-far-field boundary conditions were employed at the boundary of the computational domain. The results were compared with the experiment performed by Wilcox *et al.* (2004), and the results are shown in Fig. 4. The error in the lift coefficient was approximately 1%−3.5%, and the drag coefficient error was slightly larger, approximately 1.8%−4.5%. Therefore, the calculation model in this paper is generally accurate and the calculation results are credible.

4.3 Validation of The Turbulence Model

According to the comprehensive analysis results of different turbulence models, the DES (Detached Eddy Simulation), SAS (Scale Adaptive Simulation), and realizable models were selected for calculating the pressure-far-field incoming flow conditions. The aerodynamic data for the self-turning slender body were obtained for other turbulence models, as shown in Fig. 5. The differences in the three models, which occurred primarily in calculating the lift coefficient and the resistance coefficient, were within an acceptable range.
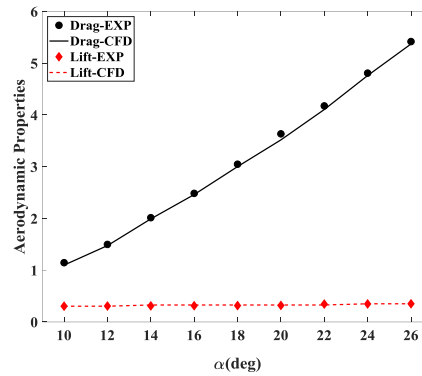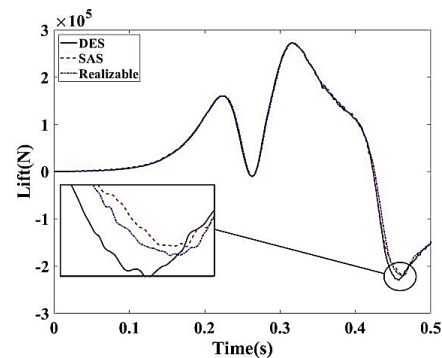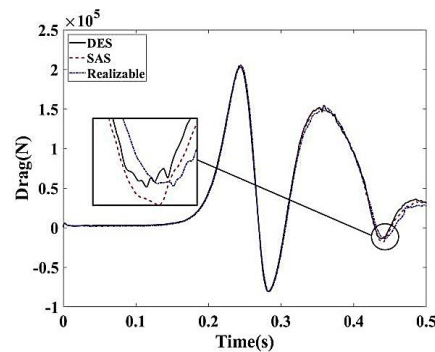

Fig. 4. Comparison between numerical results and experimental data.

(a)   Coefficient of lift

(b)   Coefficient of drag

Fig. 5. Comparison of aerodynamic coefficients of different turbulence equations.

5. RESULTS AND DISCUSSIONS

The missile body was affected by airlift, resistance, and gravity within the given pressure-far-field boundary conditions. During turning, the slender body was subjected to resistance F in the direction opposite to the velocity. It created a pitch damping moment centered around the center of gravity. The aerodynamic force formed a resultant force at the pressure center. This force produced a pitching moment centered around the center of gravity, so the selection of the center of gravity position affected the missile's overturning process. Variation trends for the primary parameters (the turning angular velocity, the aerodynamic force, the aerodynamic moment,

and the pressure center) were obtained from simulations of the entire turning process.

5.1 Position and Jump of the Pressure Center

The relative position of the pressure center was calculated by dividing the aerodynamic moment and the normal force decomposed by the aerodynamic force. Then the pressure center was investigated for different Mach numbers, and the changes in the pressure center position are shown in Fig. 6.
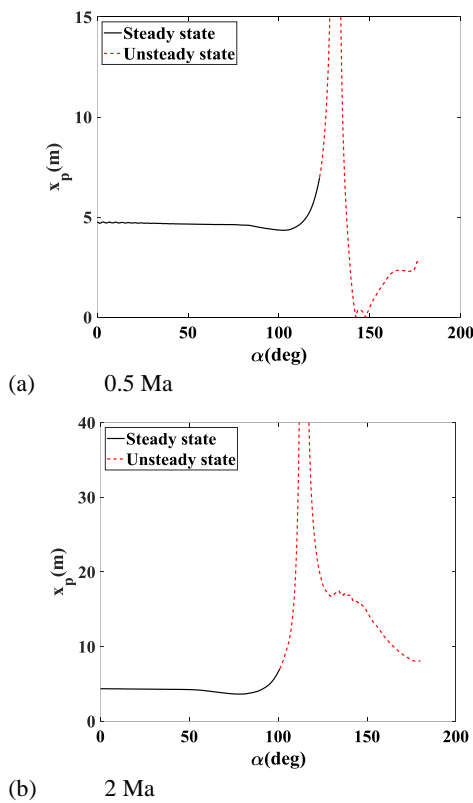

(a)   0.5 Ma

(b)   2 Ma

Fig. 6. Position of the slender body pressure center.

The positive direction of the change in the pressure center's position was along the axis of the missile body. When the angle of attack was less than 90°, the pressure center was behind the center of gravity, and the change in the pressure center position was small and relatively stable. When the angle of attack was greater than 90°, the pressure center gradually moved forward along the missile body and neared the center of gravity position. For these conditions, the pressure center position fluctuated significantly within a short time.

When the Mach number was 2, the pressure center fluctuated only once. Then the pressure center position moved forward as the angle of attack increased, and it stabilized at a fixed value. When the Mach number was 0.5, the pressure center position fluctuated more frequently as the angle of attack changed. The rate of change gradually stabilized as the angle of attack approached 180°.

When the Mach number was 0.5, the separation area of the vortex was more extensive, resulting in a more complicated flow field. When the angle of attack of the missile body was greater than a certain angle, the rotational angular velocity suddenly increased. The slender body was affected by the vortex, and the pressure center position changed drastically.

The figure shows that the singularity in the pressure center position and a pressure center location outside the projectile body appeared when the angle of attack was greater than 100°. There were two primary reasons for these results. First, the pressure center position was calculated using the ratio of the moment of the missile body to the normal force. The value of the normal force changed from negative to positive when the angle of attack was approximately 100°. At this time, the value of the denominator in the equation was minimal, so a tiny error in the normal force caused a very large error in the pressure center position, and this significant error produced a singularity. Second, a pitching moment was attached to the numerator of the equation. The calculated pressure center position was opposite to the actual pressure center position and exceeded the length of the slender body.
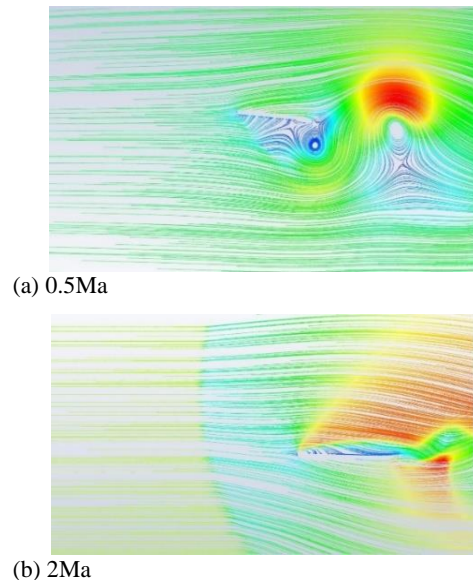

(a) 0.5Ma

(b) 2Ma

Fig.7 Comparison of velocity streamlines at different Mach numbers.
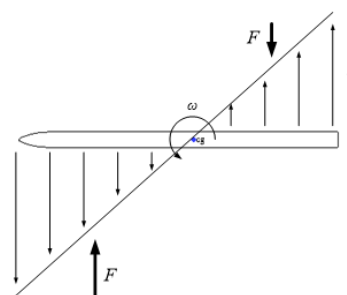

Fig. 8. Damping torque generation principle.

The slender body inevitably produced a pitch-damping moment, M_c. This damping moment was opposite to the direction of the overturning angular

velocity, and it hindered the missile body from turning. This damping moment was also one of the reasons why the turning could be stable, and not divergent.

The actual calculated moment, M, included a moment, M_F, generated by the normal force and the pitch-damping moment, M_c. Part of the pitching moment did not affect the position of the pressure center, which belonged to the moment caused by the pure couple. When calculating the pressure center position, the moment produced by the pure couple was added to the calculated moment. The formula used for calculating the pressure center is shown in Eq. (8).

$$x_P = \frac{M}{F_N} = \frac{M_F + M_c}{F_N} \qquad (8)$$

The moment generated by the force couple was always negative. When the pressure center was located behind the center of gravity, the real moments were negative. The effect of the total force couple was equivalent to making the calculated pressure center move backward relative to the actual pressure center. Therefore, the impact of the force couple may cause the calculated pressure center to exceed the missile length.

The relationship between the center of gravity position and the pressure center position is shown in Fig. 9. When the angle of attack was less than 90°, the pressure center position was forward of the center of gravity position. The normal force pointed downward, resulting in positive moments, so the rotation was accelerated. When the angle was near 90°, the pressure center position was near the center of gravity position, and the changes in the turning angular velocity tended to be gentle. When the angle was too large, the pressure center was behind the center of gravity. The normal force pointed upward, resulting in negative moments and reductions in the turning angular velocity.
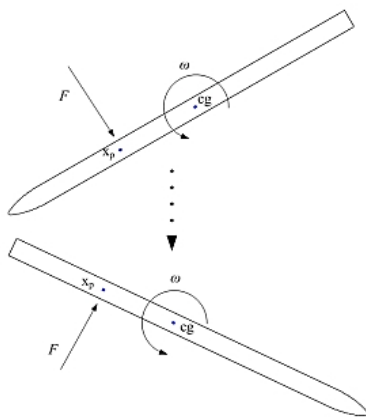

Fig. 9. Principle of self-stability caused by the pressure center movement.

5.2 Effect of The Center of Gravity Position on The Self-Turning

Considering the center of gravity position of the actual missile body, the center of gravity range was

50% to 70% of the relative length of the slender body. The simulation results show that a slender body with a center of gravity within that range could be overturned when the Mach number was 0.5. When the Mach number was 2, a slender body with a center of gravity of less than 58% could not be overturned within the set fluid domain. This result occurred because the center of gravity was distant from the pressure center in the slender body, and the slender body had strong static stability. When the Mach number was 2, the aerodynamic force on the missile body was excessive and the missile body flew quickly, so the slender body could not turn over within the fluid domain.
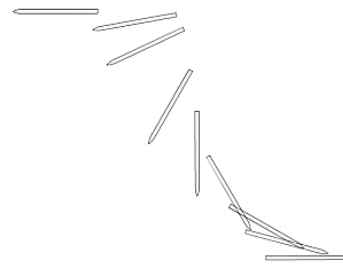

Fig. 10. Self-turning process of the slender body.

5.3 Effect of The Center of Gravity on The Turning Angular Velocity

The overturning angular velocity of the slender body is shown in Eq. (9):

$$\omega = \frac{M}{J} dt \qquad (9)$$

where J is the moment of inertia, equal to $1200 kg/m^2$.

The simulation results are shown in Fig. 11. The maximum angular velocity of the slender body gradually decreased as the center of gravity moved backward. When the angle of attack was less than 90°, the rotational angular velocity increased rapidly with the angle of attack, then the changes tended to be stable. When the angle of attack was greater than 120°, the angular velocity gradually decreased. This self-stabilization phenomenon was primarily caused by the pressure center position and the action of the pitching moment. When the attack angle was less than 90°, the pressure center was forward of the center of gravity, and the direction of the lift was downward. The direction of the moment generated by the lift was the same as the missile body overturning direction, and the moment increased the turning speed. When the attack angle was near 90°, the pressure center was near the center of gravity, the influence of the torque decreased, and the turning angular velocity tended to be stable. When the angle of attack was greater than 90°, the pressure center was behind the center of gravity and the lift direction was upward. The moment reduced the turning speed.

5.4 Effect of The Center of Gravity on the Turning Time

The turning time is defined as the time it took for the angle of attack to change from 0° to 180° during the
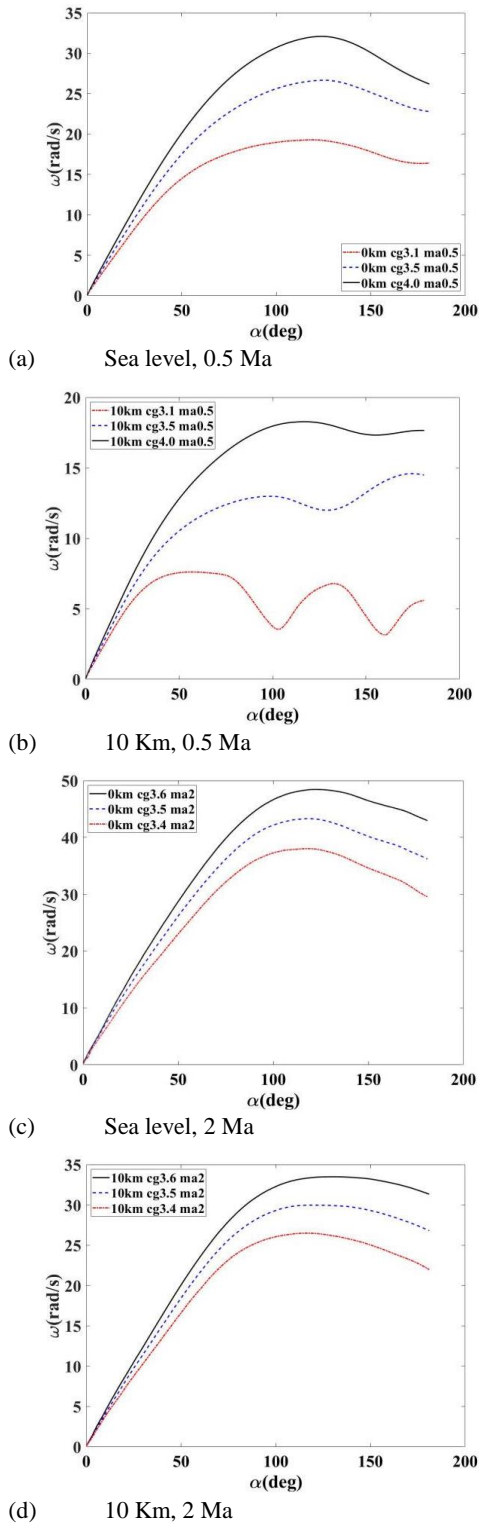
(a)　　　　Sea level, 0.5 Ma

(b)　　　　10 Km, 0.5 Ma

(c)　　　　Sea level, 2 Ma

(d)　　　　10 Km, 2 Ma

Fig. 11. Changes in the angular velocity of the slender body.

numerical simulations, and it was output to a specified file via a user-defined function. According to Fig. 12, as the center of gravity moved backward, the turning time gradually decreased. The data in Table 2 show the time required for overturning under different incoming flow conditions for the identical center of gravity positions.
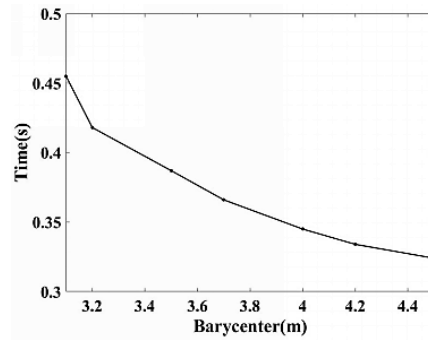

Fig. 12. Comparison of turnover times for slender bodies with different center of gravity positions.

The turning time at Mach 2 was shorter than at Mach 0.5, and the turning time at sea level was less than at 10 km. For a high Mach number, the aerodynamic force on the slender body was excessive, and the turning time was shorter. The air density and the aerodynamic force were larger at sea level than at 10 km, so the turning time was shorter. The slender body turning times for all states were within one second, which meets the overall requirements for an air-to-air missile to complete an OTS launch. This result led to the preliminary belief that the slender body could achieve adequate self-turning.

5.5 Effect of The Center of Gravity on The Normal Aerodynamic Force

The normal force is the aerodynamic force perpendicular to the axis of the missile body. The normal force was positive upward when the flip angle was less than 90° and when the attack angle was greater than 90°. As shown in Fig. 13, the peak values of the normal force for slender bodies with different center of gravity positions appeared at different attack angles. Additionally, the peak values of the normal force when the center of gravity positions were at the front were more prominent than when the center of gravity positions were at the back. During the overturning process, the normal force did not diverge, but gradually decreased to zero. At an extra-wide angle of attack, the normal force reversed, with the effects of inhibiting the overturning of the missile body, reducing the angular velocity, and gradually stabilizing the self-turning process.
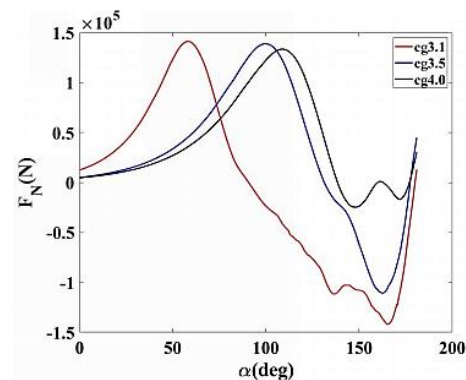

Fig. 13. Variation in the normal force.

Table 2 Slender body turnover times

Working condition	Ma=0.5，Sea level	Ma=0.5 10 km	Ma=2，Sea level	Ma=2 10 km
Time to 90° (s)	0.36	0.47	0.20	0.27
Time to 180° (s)	0.45	0.59	0.23	0.34
Turning time after theoretical control (s)	0.6668	0.8198	0.3772	0.538

The peak value of the normal force appeared earlier when the center of gravity was forward in the slender body (along the missile body direction) than when it was in the back of the slender body. Additionally, the reverse normal force value was greater after the slender body was turned and reoriented.

6. CONCLUSIONS

Based on the unsteady aerodynamic theory of slender bodies at large and extra-wide angles of attack, this study used dynamic mesh technology to study the motion of a slender body during self-turning OTS launching.

The angular velocity change, force condition, turning time, and pressure center position change of the missile body's center position were analyzed. The feasibility of the self-turning launching was verified, and the following five primary conclusions were obtained.

1) The hysteresis effect of a slender body with an extra-wide angle of attack on the flow field caused a pressure center jump phenomenon. Additionally, the pressure center was located outside the missile body. The position change of the pressure center caused the overturning angular velocity to self-stabilize. These results provided a research basis for similar types of aerodynamic shape research.

2) During the overturning process, the slender body experienced a self-stabilization phenomenon. When the turning angular velocity changed, it did not always increase to divergence, but grew to a certain value and then decreased. At a Mach number of 2, the maximum angular velocity reached 48.44 rad/s and the final angular velocity was 42.98 rad/s. At a Mach number of 0.5, the maximum angular velocity was 32.08 rad/s and the final angular velocity was 26.26 rad/s. The self-turning process of the slender body was more stable at the lower Mach number. The emergence of the self-stabilization phenomenon was due to the dual effect of the pressure center position change and a pitch-damping moment.

3) A center of gravity selection range for the self-turning OTS launching technology was verified, and at a Mach number of 0.5, the center of gravity selection range for the slender body was more extensive. The center of gravity selection range at Mach 2 was 8% less than at Mach 0.5. The center of gravity position range selected for a conventional missile body could meet the self-turning launch requirements for the center of gravity location.

4) When the center of mass moved forward along the missile body, the peak value of the turnover angular velocity increased gradually, and the turning time decreased. At a Mach number of 2, the average time was 0.52 s. At a Mach number of 0.5, the average time was 0.29 s. The times for the various working conditions were within one second, which meets the design requirement for OTS launching.

5) The peak value of the normal aerodynamic force in the positive direction did not increase as the center of gravity moved. The peak value of the normal force after turning increased gradually as the center of gravity moved forward.

REFERENCES

Barnette, D., M. Bettencourt and M. Hoemmen (2012). Using miniapplications in a Mantevo framework for optimizing Sandia's SPARC CFD code on multi-core, many-core, and GPU-accelerated compute platforms. In 51st AIAA aerospace sciences meeting including the new horizons forum and aerospace exposition (p. 1126).

Bellakhal, G., J. Chahed and F. Chaibina (2019). First and second order turbulence closures applied to homogeneous turbulent bubbly flows. *Journal of Applied Fluid Mechanics* 12(6), 1813-1823.

Cao, Y., W. Tan, Y. Su, Z. Xu and G. Zhong (2020). The Effects of Icing on Aircraft Longitudinal Aerodynamic Characteristics. *Mathematics* 8(7), 1171.

Champigny, P. (1986). Stability of side forces on bodies at high angles of attack. *4th Applied Aerodynamics Conference* (p. 1776).

Deng, X., Q. Chen, X. Yuan and J. Chen (2016). Study of aerodynamic uncertainty on the complex slender vehicle at high angle of attack. *Scientia Sinica Technologica* 46(5), 493-499.

Hechmi, K. and L. Taieb (2012). An extension of the ssg model on compressible turbulent flow. *Journal of Applied Fluid Mechanics* 5(4), 101-111.

Howison, J. and K. Ekici (2013). Unsteady Analysis of Wind Turbine Flows Using the Harmonic Balance Method. *Aiaa Aerospace Sciences Meeting* (p. 1107).

Kang, D. H. and O. J. Kwon (2020). Numerical study about buffet characteristics and attenuation of vertical tail at high angles of attack. *International Journal of Aeronautical and Space Sciences* 21(2), 315-328.

Le Clainche, S., D. Rodríguez, V. Theofilis and J. Soria (2016). Formation of three-dimensional structures in the hemisphere-cylinder. *AIAA Journal* 54(12), 3884-3894.

Li, H., S. Guo, Y. L. Zhang, C. Zhou and J. H. Wu (2017). Unsteady aerodynamic and optimal kinematic analysis of a micro flapping wing rotor. *Aerospace Science and Technology* 63, 167-178.

Liu, Y., R. W. Claus, J. S. Litt and T. H. Guo (2013). Simulating Effects of High Angle of Attack on Turbofan Engine Performance. *51st AIAA Aerospace Sciences Meeting including the New Horizons Forum and Aerospace Exposition* (p.1075).

Ma, Q. and H. Li (2020). Design of Attitude Control Law for Over-Shoulder Launch of Helicopter-borne Air-to-ground Missile. *In 2020 IEEE 5th Information Technology and Mechatronics Engineering Conference (ITOEC)* (pp. 1620-1625). IEEE.

Menter, F. R. (1994). Two-equation eddy-viscosity turbulence models for engineering applications. *AIAA Journal* 32.

Qi, Z., Y. Wang, H. Bai, Y. Sha and Q. Li (2018). Effects of micro-perturbations on the asymmetric vortices over a blunt-nose slender body at a high angle of attack. *European Journal of Mechanics-B/Fluids* 68, 211-218.

Sulaeman, E., A. Omar, W. Asrar, M. Aldheeb and A. Altaf (2019). Effect of a Directionally Porous Wing Tip on Tip Vortex. *Journal of Applied Fluid Mechanics* 13(2), 651-665.

Teng, J., J. Zhang, Z. An and Y. You (2018). Detached eddy investigation of conical cavity flow at Mach 0.9. *Journal of Applied Fluid Mechanics* 11(1), 165-176.

Thukral, A. and M. Innocenti (1998). A sliding mode missile pitch autopilot synthesis for high angle of attack maneuvering. *IEEE Transactions on Control Systems Technology* 6(3), 359-371.

Tong, H., J. Fang, J. Guo, K. Lin and Y. Wang (2019). Numerical simulation of unsteady aerodynamic performance of novel adaptive airfoil for vertical Axis wind turbine. *Energies* 12(21), 4106.

Wang, X., W. Zhengwei, U. Wenjun (2021) Analysis on Flowfield and Aerodynamic Characteristics of Escort Free-Flight Decoy with Asymmetrical Tail at High Incidences. *Journal of Ordnance Equipment Engineering* 42(03), 55－60, 82.

Wilcox, F., T. Birch and J. Allen (2004). Force, surface pressure, and flowfield measurements on a slender missile configuration with square cross-section at supersonic speeds. *In 22nd Applied Aerodynamics Conference and Exhibit* (p. 5451).

Yang, L., M. Wang and Z. Gao (2011). Numerical investigation of unsteady aerodynamic characteristics of a pitching missile. *Aerospace Science and Technology* 15(2), 129-136.

Zhu, Y., H. Yuan and C. Lee (2015). Experimental investigations of the initial growth of flow asymmetries over a slender body of revolution at high angles of attack. *Physics of Fluids* 27(8), 246-257.